Bachelor Thesis

Analysis of the $b_1(1235)\pi$ Final State in COMPASS Data

Markus Ebert

July 24, 2011

Physik Department E18
Technische Universität München

Contents

1 Introduction

Quantum chromodynamics (QCD) is the well-established theory for the strong interaction. There is no evidence that this theory needs to be extended. In contrast there are even several phenomena allowed by QCD that have not yet been observed or verified.

In the low-energy region, QCD calculations suffer from the running coupling constant α_s which makes perturbation theory not applicable. Instead methods like lattice QCD or chiral perturbation theory have to be applied. These calculations and QCD-inspired models have shown that particles could exist which cannot be explained with the successful constituent quark model. Although this model was able to explain the richness of the observed hadron spectrum and some of the hadron properties, it is only applicable to quark-antiquark-combinations (mesons) or 3-quark-particles (baryons), inherently constraining fundamental properties like spin and parity or charge conjugation eigenvalues. Particles outside of this framework are commonly referred to as "exotics", reflecting that their quantum numbers cannot be explained by the constituent quark model. A particular interesting class are "spin-exotic" mesons which have spin, parity and C-parity quantum numbers forbidden for $q\bar{q}$-mesons. An explanation for the existence of such mesons could be the excitation of gluonic degrees of freedom. The gluonic selfinteraction might even lead to mesonic states purely consisting of gluons, so called "glueballs". Other candidates for exotic mesons are mesonic molecules (mesons bound together similar to atoms, but through strong interaction), multi-quark states and hybrid mesons ($q\bar{q}$-mesons with valence gluons).

The lowest mass spin-exotic hybrids are predicted in the mass region around $2\,\mathrm{GeV/c^2}$. The flux-tube model predicts the lightest hybrid with quantum numbers $J^{PC} = 1^{-+}$ to decay primarily to $b_1\pi$[1]. This decay channel has already been investigated at the BNL experiment E852 in 2005 and was found to contain the spin-exotic states $\pi_1(1600)$ and $\pi_1(2000)$[1]. The $\pi_1(1600)$ was also found in a partial-wave analysis of the $b_1\pi$-channel at the VES experiment[2]. However these results have not yet been verified and are still disputed[3]. The COMPASS experiment has collected an excellent data sample during the 2008 and 2009 runs which will allow to verify these observations.

The purpose of this thesis is to reconstruct the decay channel $\pi^- p \to Xp \to (b_1(1235)\pi)p$ from the diffractive pion scattering off protons. The resulting mass distribution of the unknown intermediate state X can then be used in a following partial-wave analysis to identify the resonances contributing to this decay channel and hopefully verify the existence of the expected spin exotic particles.

2 The COMPASS Experiment

The unique feature of the COMPASS experiment (**CO**mmon **M**uon and **P**roton **A**pparatus for **S**tructure and **S**pectroscopy) is that it can perform measurements using both a muon and a hadron beam. This thesis is based on the hadron program which uses a pion beam. The fundamental aspects of the experimental setup, shown in figure 2.1, are briefly explained in the following chapters. Detailed descriptions can be found e.g. in [4, 5].

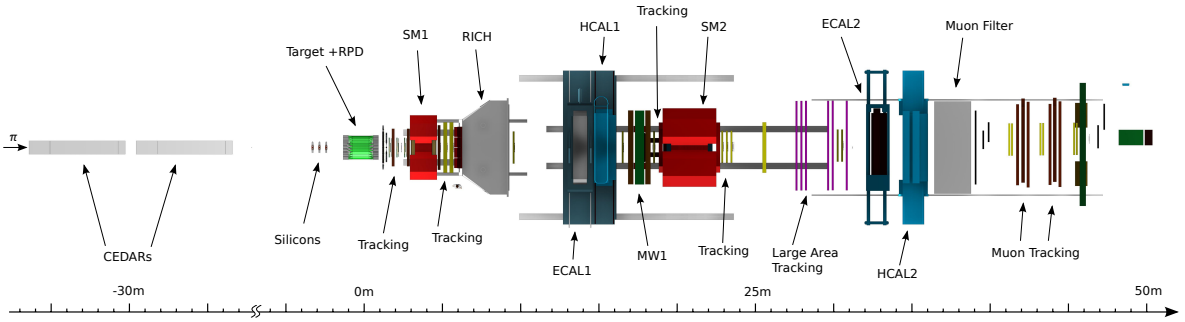

Fig 2.1: Setup of the COMPASS experiment[6]

2.1 The M2 Beam Line

COMPASS is connected to the **S**uper **P**roton **S**ynchroton (SPS) at CERN which delivers a 400 GeV/c proton beam. During the 4.8s long spills within the 16.8s long SPS cycle, about $1.2 \cdot 10^{13}$ protons are impinging on a Beryllium target, thereby creating secondary particles, mainly pions and kaons. Using several magnets, the beam is guided to the experiment. At arrival, the negative hadron beam consists of 95% pions and 4.5% kaons with a beam momentum of about 190 GeV/c[4]. These particles can be tagged using a pair of Cherenkov counters (CEDAR detectors).

2.2 The Proton Target

The target consists of liquid hydrogen cooled by liquid Helium. The cylindrical target cell has a diameter of 3.5 cm and a length of 40 cm[7]. Figure 2.2 shows the setup in the target region.

Detecting the recoiled proton is essential for the analysis of diffractive processes. Therefore a Recoil Proton Detector (RPD) is installed around the target. “The RPD

consists of two cylindrical scintillator rings A and B. Ring A is phi-segmented in 12 parts, ring B phi-segmented in 24 parts. Both rings surround the liquid hydrogen target, A in a distance of 120mm, B in a distance of 775mm from the target center. The A scintillators are 500mm long and 5mm thick, whereas the B scintillators have a length of 1080mm and have a thickness of 10mm. "[8] This geometry, shown in figure 2.3, yields an azimuthal resolution of the order of 15° and a scattering angle coverage by the slates of 55° to 90°.

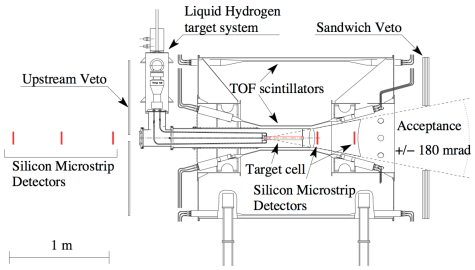

Fig 2.2: Target setup[9]

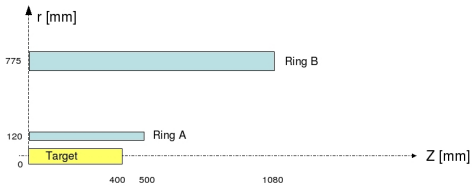

Fig 2.3: RPD arrangement[8]

2.3 Particle Tracking

Particle tracking at COMPASS is divided into three parts according to the radial distance to the beam axis[4]: **V**ery **S**mall **A**rea **T**racking (VSAT) for distances lower than $2.5 - 3\,\text{cm}$, **S**mall **A**rea **T**racking (SAT) up to $30 - 40\,\text{cm}$ from the beam and **L**arge **A**rea **T**racking (LAT).

In the VSAT region, a high time and spatial resolution as well as radiation hard materials are needed due to the high beam intensities. The silicon microstrip detectors arranged in this region are used to track the beam and reconstruct the primary vertex.

The SAT region is covered by so-called GEM and Micromegas detectors (cf. [4]) which are based on the ionization of a gas by charged particles. These devices also have a good resolution and are chosen for their lower costs with respect to silicon detectors.

In the LAT area drift chambers and multiwire proportional counters are used.

2.4 Spectrometers

COMPASS contains two spectrometers, each consisting of a bending magnet followed by tracking devices and an electromagnetic and a hadronic calorimeter. The devices are shown in figure 2.1: The **L**arge **A**ngle **S**pectrometer (LAS) with an polar angle acceptance up to 180 mrad consists of SM1, ECAL1 and HCAL1, the **S**mall **A**ngle **S**pectrometer (SAS) consists of SM2, ECAL2 and HCAL2 [5]. The electromagnetic calorimeters measure the energy of particles mainly interacting electromagnetically like electrons and photons. Hadrons can pass these detectors with low energy losses and are detected in the adjacent hadronic calorimeter.

Electromagnetic calorimeters (ECal) In the high-energy regime covered by the ECals photons interact mainly via pair production. Charged particles, including electrons and positrons from pair production, emit bremsstrahlung photons which can in turn induce pair production. This cascade of bremsstrahlung and pairproduction continues until the threshold for e^+e^--creation is reached, thus causing an electromagnetic shower[10].

At COMPASS two possibilities to measure these showers are used. SHASHLIK modules contain about 150 alternating layers of lead and scintillators. The showers are detected by the scintillation light caused by bremsstrahlung photons. Several wavelength shifting fibres are inserted to transport the light to photomultipliers[7]. The other type uses lead glass, a mixture of PbO and SiO_2, to induce the showers which are measured by detecting the Cherenkov radiation emitted by electrons and positrons from pair production again with photomultipliers. Three different variants of lead glass blocks (GAMS, MAINZ and OLGA) are used at COMPASS. They differ in material composition and length.

Figure 2.4 shows the setup of both calorimeters. ECal2 consists of radiation hard SHASHLIK and GAMS-modules which are necessary due to the large intensity of high-energy particles. At ECal1 only the inner modules around the opening for the small angle particles need to be radiation hard.

A photon hitting a calorimeter cell usually results in an electromagnetic shower distributed over several modules which are combined to a cluster. In cases like the $\pi^0 \to \gamma\gamma$ decay, the two photons are usually emitted with a small angle. If this angle is too small, the clusters overlap and can not be distinguished.

Both ECals are calibrated using an electron beam with well-defined energy from SPS, but as shown in the analysis, the calibration still needs improvement. An online calibration during measurements is provided by a laser monitoring system (cf. [10]).

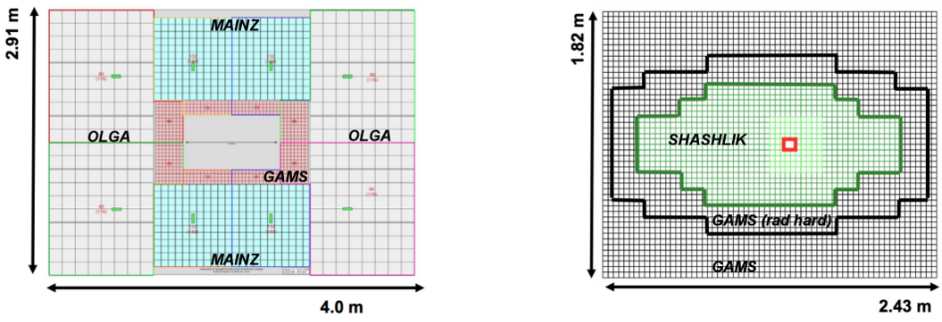

(a) ECal1 (b) ECal2

Fig 2.4: Setup of the electromagnetic calorimeters (Adapted from [6])

Hadronic calorimeters (HCal) The hadronic calorimeters consist of layers of steel and scintillators. Hadrons interact strongly in the material and create a cascade of particles, thereby causing scintillation light that can be measured by photomultipliers attached to wavelength shifting fibres[4].

3 Data Analysis

3.1 Reconstruction of the $b_1(1235)\pi$ Final State

At the COMPASS experiment diffractive pion scattering off a stationary proton target is investigated. At high beam energies, the proton acts only as a strong interaction partner and stays intact, as long as small momentum transfer is considered; the incoming pion is excited to a resonance and finally decays into several particles[11].
This thesis focuses on the analysis of intermediate states X decaying as

$$\pi^- p \to Xp \to (b_1(1235)^0\pi^-)p \tag{3.1}$$

$$\pi^- p \to Xp \to (b_1(1235)^-\pi^0)p \tag{3.2}$$

In the following only decay 3.1 is considered. The corresponding reactions for 3.2 result from exchanging the $b_1(1235)^0$ and π^- charge. The final state measured in the detector is identical.
The neutral $b_1(1235)^0$ decays predominantly via [12]

$$b_1(1235)^0 \to \omega + \pi^0 \tag{3.3}$$

The ω has a lifetime of $\tau_\omega = 7.75 \cdot 10^{-23} s$[12] and decays practically instantaneously via

$$\omega \to \pi^+ + \pi^0 + \pi^- \tag{3.4}$$

with a branching fraction of 89.1% [12]. The total $b_1(1235)^0$ decay chain thus reads as

$$b_1(1235)^0 \to \omega + \pi^0 \to \pi^+ + \pi^0 + \pi^0 + \pi^- \tag{3.5}$$

The very short-lived π^0 with a mean life time of $8.4 \cdot 10^{-17} s$ [12] also decays virtually immediately via

$$\pi^0 \to \gamma + \gamma \tag{3.6}$$

The charged pions can only decay via the weak interaction and have a mean decay length of $c\tau_{\pi^\pm} = 7.8\,\mathrm{m}$[12]. Multiplied with the Lorentz factor $\beta\gamma$, the high energetic pions have a decay length much larger than the length of the spectrometer, so these particles are considered as quasi-stable. Thus the net reaction considering the finally measured particles is

$$\pi^- + p \to \pi^+ + 2\pi^- + 4\gamma + p_{Recoil} \tag{3.7}$$

3.2 Analysis Software

At COMPASS, the raw data recorded by the detectors is processed in the following steps[13]:

- First the raw data is decoded.
- Using a database the information from the detector channels is converted into a set of hits in space and time.
- The hit information together with additional setup data are then processed by the CORAL software[14], which reconstructs charged particle trajectories (track) and possible interaction points (vertices) and stores them as ROOT-files. The reconstructed events contain all particles, tracks, vertices etc. which were found to be associated with a single reaction. ROOT is a general-purpose object-oriented C++ framework developed at CERN to handle and analyse large quantities of data[15].
- Finally these files are processed using the PHAST software which performs the actual analysis[16].

3.3 Event Selection

In order to analyze the $b_1(1235)\pi$ final state it is necessary to select events with the correct signature. Most parts of this event selection were adapted from [7] and [10]. The investigated data sample was recorded in period W37, 2008 run, slot 3 production. In the following the selection cuts are described in more detail.

DT0-Trigger The **D**iffractive **T**rigger DT0 is a hadron trigger used to exclude non-diffractive processes. It consists of the following individual trigger systems[17]:

- Beam Trigger: The Beam trigger ensures that the track of a beam particle leading into the target was recognized.
- **R**ecoil **P**roton **D**etector (RPD): The RPD ensures that a recoil proton was detected.
- Veto Trigger: "The task of the Veto system is to veto on secondary particles coming from hadronic interaction in the beamline, Halo particles, non-interacting particles and interactions going outside the angular acceptance of the COMPASS spectrometer to guarantee exclusivity"[17]

Exactly one primary vertex The **P**rimary **V**ertex (PV) is defined as the point at which the interaction between incoming beam particle and target proton occurs. In case of reactions happening nearly at the same time, it is possible to associate more than one primary vertex with an incoming track. Thus a cut on exactly one recognized primary vertex is necessary.

Location of primary vertex Beam particles do not only react with the proton target but also with the surrounding detectors and target construction. The background from these reactions is filtered by requiring that the reconstructed primary vertex is located in the target volume.

The preselection cut restricts the location of the vertex to $-80\,\mathrm{cm} \leq z \leq -20\,\mathrm{cm}$. The final cut on the actual target location $-69\,\mathrm{cm} \leq z \leq -29\,\mathrm{cm}$ and $r \leq 1.5\,\mathrm{cm}$ is performed later before cutting on the physical properties of the event (see table 3.1 for a cut overview).

The result of these second cuts are shown in figure 3.1. Obviously the distribution of events is not uniform in the target area due to scattering of the produced pions inside the target which disturbs the reconstruction of events further upstream. Particles from events at higher values of z have a smaller path inside the target and thus lower probability to scatter. Furthermore the beam itself has no homogeneous distribution, as can be seen in the radial view which also clearly shows the fill level of the target and the surrounding vessel.

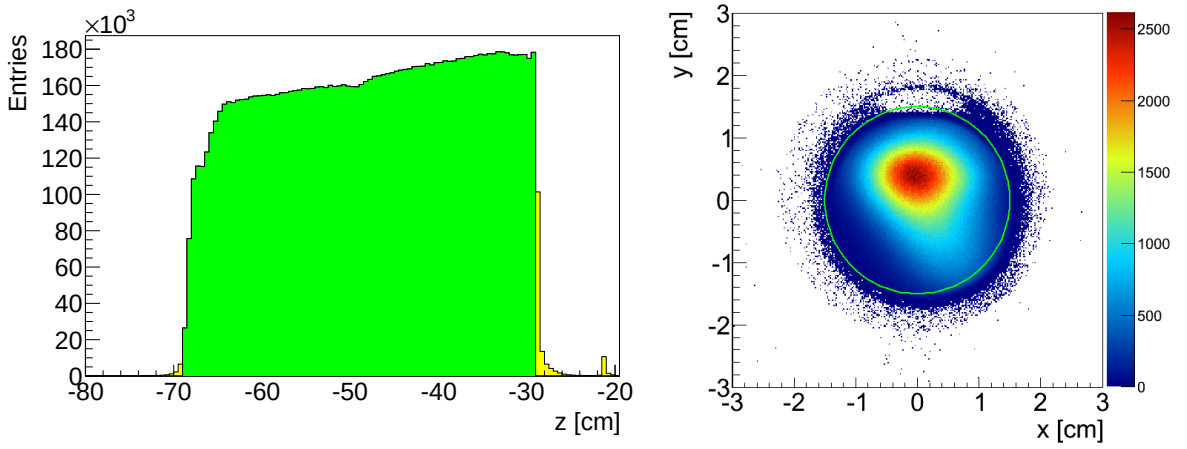

(a) z-distribution of the primary vertex location

(b) Radial distribution of the primary vertex location

Fig 3.1: Location of the primary vertex. The results of the final cuts on $-69\,\mathrm{cm} \leq z \leq -29\,\mathrm{cm}$ and $r \leq 1.5\,\mathrm{cm}$ are shown in green.

Identification of incoming particle In principle, the kaonic beam component can be eliminated using the CEDAR information. At the current status, the CEDAR information can only be used to tag parts of the beam with a small inclination with respect to the nominal beam axis. For this reason the CEDAR information is not used in this analysis.

Recoil Proton Detector Detecting the recoiled proton is necessary to ensure diffractive scattering. Measuring its momentum and energy also allows to reduce non-exclusive events by checking the energy and momentum balance.

Outgoing particles The detected final state particles have to meat the following conditions:

- Exactly one positively charged particle (π^+) was detected.
- Exactly two negatively charged particles (π^-) were detected.
- Exactly four good photons were detected.

  These photons must be correlated with the primary vertex, which was guaranteed by cutting on the time difference of the photon cluster in the calorimeter and the beam time: $|t_{Beam} - t_{Ecal}| \leq 5\,\text{ns}$. This cut is shown for ECal2 in figure 3.2.

  To exclude signals from electronic noise in the calorimeters, only clusters with a minimum energy of 1 GeV (ECal1) and 4 GeV (ECal2) are allowed.

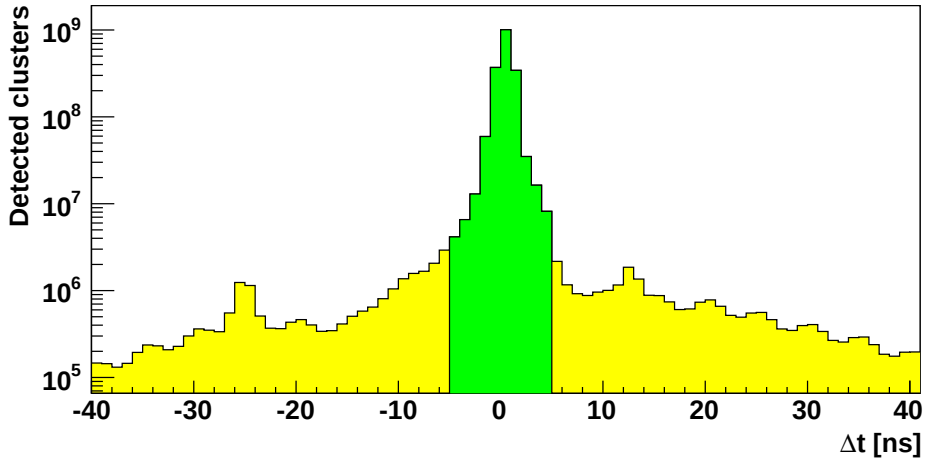

Fig 3.2: Number of detected gammas with minimum energy of 4 GeV against the time difference between primary vertex and detected clusters in ECal2 . The cut $\Delta t = |t_{Beam} - t_{Ecal}| \leq 5\,\text{ns}$ is shown in green.

Photon calibration As will be shown in the π^0-reconstruction (chapter 3.4), the calibration of the electromagnetic clusters is insufficient. Therefore Tobias Schlüter developed a preliminary calibration of the reconstructed calorimeter clusters[18, 7]: Using a large dataset, events with a 2γ invariant mass near the π^0-mass were selected. For these events correction factors were calculated to push the measured invariant mass to the correct π^0-mass. These values are stored for the cells with the highest energy deposit in each cluster. After processing all events, the mean value of these factors is calculated. Iterating this process leads to a table of correction factors.

To calibrate the detected clusters, the cell containing the highest energy in each cluster is determined. The precalculated correction factor for this cell is then applied to the cluster energy.

Recoil proton momentum

Exclusive events can be enriched by demanding that the momentum bilance $\vec{p}_{\pi^-} = \vec{p}_p + \vec{p}_X$ is approximately fulfilled. Since the proton momentum is measured not very precisely by the RPD (see chapter 2), directly verifying this equation is not possible. Instead only the transverse momentum is checked. The following cuts are shown in figure 3.3.

The momenta of the recoil proton and the intermediate state X are projected in the plane perpendicular to the momentum of the beam particle. Due to momentum conservation, these projections should be antiparallel. Expressed in terms of azimuthal angles around the beam axis, the cut was performed as $160° \leq |\phi_p - \phi_X| \leq 200°$.

Another cut was performed by measuring the projection of the proton momentum onto the reaction plane, spanned by the beam particle and the intermediate state X. This cut is also sensitive on transverse momentum conversation because in case of momentum conservation, the incoming and both outgoing particles (intermediate state X and proton) should move in the same plane. The condition was set to $|p_{p\perp}| \leq 0.1\,\mathrm{GeV}/c$.

Finally the magnitudes of both transverse momenta with respect to the beam were checked. The quantity $\Delta p_T = |p_{T,p}| - |p_{T,X}|$ turned out to be slightly asymmetric. The cut was applied as $-0.4 \leq \Delta p_T \leq 0.2\,\mathrm{GeV}/c$.

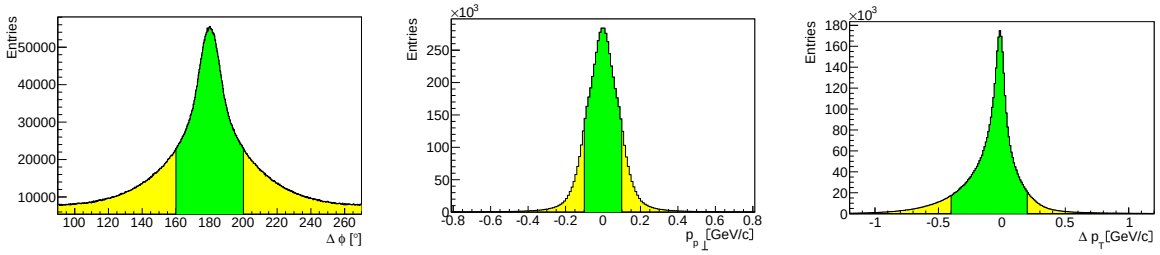

(a) Difference of azimuthal angle $\Delta\phi = |\phi_p - \phi_X|$

(b) Proton momentum component perpendicular to reaction plane $p_{p\perp}$

(c) Difference of transverse momenta $\Delta p_T = |p_{T,p}| - |p_{T,X}|$

Fig 3.3: RPD cuts on the momenta of recoil proton and intermediate state X. The cuts are shown in green.

Exclusivity

An exclusive measurement can also be verified by checking that the energy sum of all outgoing particles equals the energy of the incoming pion. Because measuring the beam energy would disturb the beam due to interactions with detector material, the energy is known not very precisely: $E_{Beam} = (191 \pm 2)\,\mathrm{GeV}$ [7]. Also taking into account the resolution of the spectrometers, the cut can not be chosen very restrictive and was applied as $180\,\mathrm{GeV} \leq E_{total} \leq 200\,\mathrm{GeV}$. This cut is presented in figure 3.4. The comparison with the total energy distribution before applying the RPD cuts described in the paragraph above indicates their good background suppression.

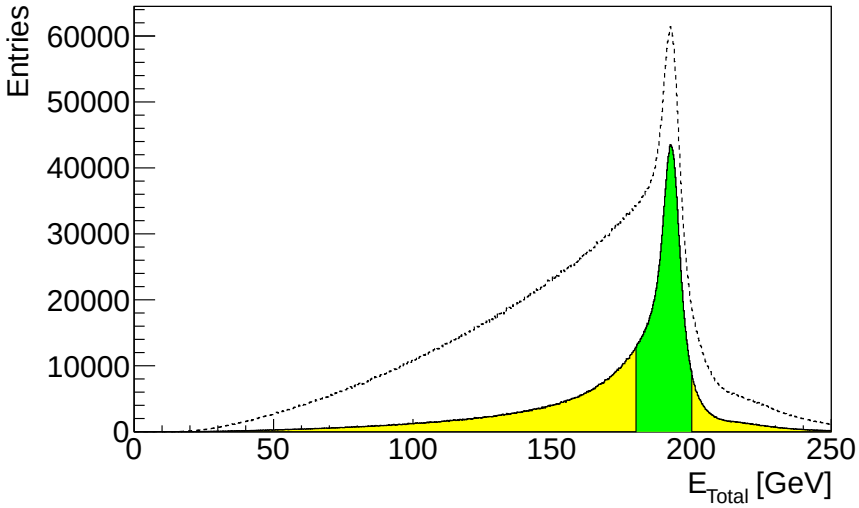

Fig 3.4: Cut on the total energy of the detected particles. The green area represents the cut on $180 \leq E_{total} \leq 200\,\text{GeV}$. The dashed line shows the spectrum before applying the RPD cuts.

Summary of the event selection Table 3.1 shows the results after applying the described filters on the original data set. Only about 0.07% of all detected events had the correct signature for the considered 5π final state. This explains the low statistics despite the large dataset that will be observed in the analysis.

Cut	**Events**	**Percentage**
Total	$2.82 \cdot 10^9$	100%
DT0-Trigger	$2.07 \cdot 10^9$	73.1%
Exactly one PV	$1.67 \cdot 10^9$	59.0%
Location of PV: $-80\,\text{cm} \leq z \leq 20\,\text{cm}$	$1.52 \cdot 10^9$	53.7%
Exactly one recoil proton	$1.09 \cdot 10^9$	38.5%
One outgoing positive particle	$2.28 \cdot 10^8$	8.07%
Two outgoing negative particles	$1.36 \cdot 10^8$	4.81%
Four good photons after calibration	$1.29 \cdot 10^7$	0.46%
Location of PV: $-69\,\text{cm} \leq z \leq 29\,\text{cm}$	$1.27 \cdot 10^7$	0.45%
Location of PV: $r \leq 1.5\,\text{cm}$	$1.26 \cdot 10^7$	0.44%
RPD: Azimuthal angle: $160° \leq \lvert\Delta\phi\rvert \leq 200°$	$5.89 \cdot 10^6$	0.21%
RPD: Proton momentum: $\lvert p_p^{\perp}\rvert \leq 0.1\,\text{GeV}/c$	$4.36 \cdot 10^6$	0.15%
RPD: Transverse momenta: $-0.4 \leq \Delta p_T \leq 0.2\,\text{GeV}/c$	$3.69 \cdot 10^6$	0.13%
Exclusivity: $180 \leq E_{total} \leq 200\,\text{GeV}$	$1.92 \cdot 10^6$	0.07%

Table 3.1: Amount of events after each cut as total number and relative percentage. The values were rounded to three digits.

3.4 Particle Reconstruction

Reconstructing the resonance decay chain is performed in the following steps:

- Construct the $2\pi^0$-system from the four measured photons. Only events with exactly one good combination are allowed.
- Apply kinematic fitting to correct the π^0 mass.
- Select the $\pi^+\pi^0\pi^-$-system resulting from the ω-decay. Only events with exactly one good combination are allowed.
- The remaining π^0 and π^- can be associated to

$$b_1(1235)^0\pi^- \to (\omega\pi^0)\pi^- \quad \text{or} \quad b_1(1235)^-\pi^0 \to (\omega\pi^-)\pi^0$$

π^0 Reconstruction There are three possibilities to build a $2\pi^0$-pair out of four photons, thus resulting in a combinatorial background. For each of these $(2\gamma)(2\gamma)$-combinations, the 2γ invariant masses are calculated and compared with the π^0-mass of $135.0\,\mathrm{MeV/c^2}$[12]. To exclude ambiguities, only events where exactly one combination satisfies the assumption of being a $2\pi^0$-system are retained.

This was achieved by cutting on the 2γ invariant mass. The parameters for this cut were estimated by fitting the 2γ invariant mass spectrum. Because the width is merely due to the resolution of the calorimeters, a Gaussian fit on top of a second order polynomial background is chosen. The fit range is $100 \leq m_{2\gamma} \leq 170\,\mathrm{MeV/c^2}$. Using the obtained standard deviation of the Gaussian fit, a 2σ-cut is performed.

Figure 3.5 shows the 2γ invariant mass spectrum including fit and cut. The grey area shows the cut range, the green area represents events where exactly one $(2\gamma)(2\gamma)$-pair fulfilled this cut. The large difference is mostly due to $(2\gamma)(2\gamma)$-combinations where only one photon pair fulfilled the cut. Only about 0.8% of the events had more than one good $2\pi^0$ reconstruction and were thus excluded. The cut is also illustrated by plotting the masses of both photon pairs against each other. The fit results are shown in table 3.2. These fits also show the benefits of the calibration described in chapter 3.3: The difference of the reconstructed masses to the correct mass as well as the width decrease significantly.

	Mean ($\mathbf{MeV/c^2}$)	**Sigma ($\mathbf{MeV/c^2}$)**
Uncalibrated	137.4	7.0
Calibrated	135.9	5.6
PDG[12]	135.0	$\approx 8 \cdot 10^{-6}$

Table 3.2: Fit results of the 2γ invariant mass using a Gaussian signal on top of a second order polynomial background for uncalibrated and calibrated data. The values are rounded to the precision of the fit result.

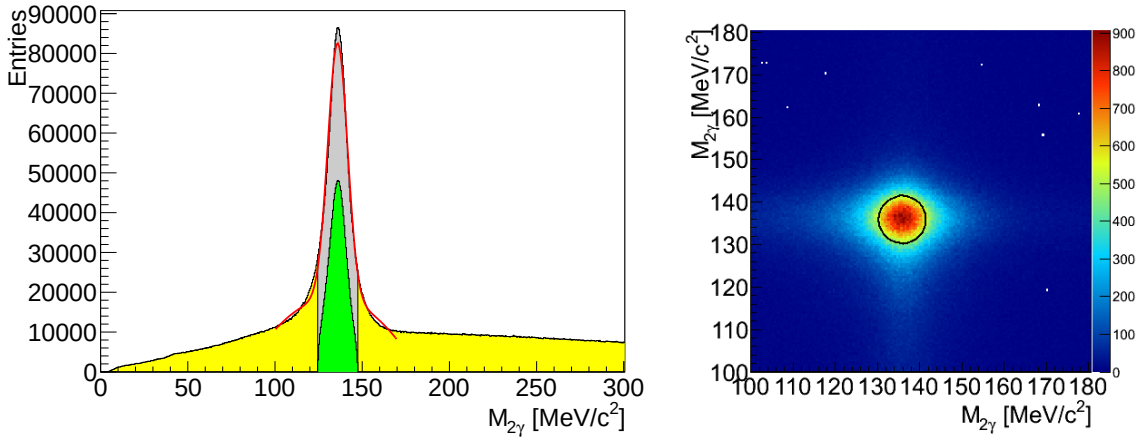

(a) (b)

Fig 3.5: Invariant mass of the photon pairs for the π^0 reconstruction.
a) The mass of both pairs plotted in the same histogram (6 entries per event). Fitting the spectrum (red) yields the cut range for good photon pairs (grey). The green part marks the actually cutted events.
b) Invariant mass of the two photon pairs plotted against each other (3 entries per event). The black circle represents the cut derived in a).

Kinematic Fitting Assuming a 2γ-pair resulted from a π^0-decay, it is possible to use the actual π^0-mass instead of the measured invariant mass in order to improve the exclusivity peak and the ω-mass (see below). Kinematic fitting is used to correct the Lorentz vectors of both photons in order to shift the invariant mass to the correct π^0-mass. This kinematic fit was implemented by Tobias Schlüter[19].

In general the quality of this fitting mechanism can be judged by two values:

- Confidence Level: "The confidence level is the probability that a χ^2 higher than the one observed would occur"[19]. If the hypothesis is true, a flat distribution with a peak around zero should occur, where the peak near zero results mostly from photons unlikely to result from a π^0-decay. In principal cutting on this peak would reject events with a high probability of failing the constraint.

- Pulls: The pulls are defined as $p_i = \frac{\eta_i - y_i}{\sqrt{C_{ii} - C'_{ii}}}$, where y_i is the measured value, η_i the constrained value and C_{ii} and C'_{ii} the quadratic error σ^2 of the measured quantity before and after the fit[7]. "One expects each of the p_i to be distributed following a Gaussian distribution of width one, centered about zero. Deviations from this Gaussian shape then point towards bad estimation of the errors of the measured data. If the distributions are not centered about zero, this may point towards systematic overestimation or underestimations of the respective quantities."[19]

For a cluster described by the measured energy E and its position (X, Y, Z), the quantities to be fitted are E, $x = \frac{X}{R}$ and $y = \frac{Y}{R}$ with $R = \sqrt{X^2 + Y^2 + Z^2}$. There is no

need to fit z because the invariant mass depends only on the angle between the photons which is determined by x and y, but not directly on the cluster position[19].

The kinematic fit was applied to all previously selected π^0. The obtained confidence level is shown in figure 3.6, the pulls in figure 3.7. The confidence level exhibits no prominent peak around zero which can be explained by the suppression of photon pairs unlikely to result from a π^0-decay during the calibration, as without calibration this peak was much clearer. For this reason a cut on the confidence level is not performed. The pulls show a slight deviation from the expected Gaussian form because the error estimates from the calorimeters are not very precise. Furthermore, the calibration shifts the cluster energies but not the associated error which results in a small error miscalculation.

ω Reconstruction Having reconstructed the $\pi^+2\pi^02\pi^-$-system, there are four possibilities to associate a $\pi^+\pi^0\pi^-$-subsystem with the assumed ω-decay. Similar to the π^0-treatment, the invariant masses for all possibilities were calculated and fitted. In contrast to the 2γ-fit a Gaussian distribution is not applicable because the peak width is of the same order as the natural decay width of $\Gamma_\omega = 8.4\,\mathrm{MeV/c^2}$. Instead a Voigt profile, a convolution of a Lorentz and Gaussian profile, on top of a second order polynomial is used. A Voigt profile contains two widths, the standard deviation σ of the Gaussian profile and the width Γ of the Lorentz curve. The full width at half maximum $\Gamma_{\mathrm{FWHM,\ Voigt}}$ can be calculated only approximately as

$$\Gamma_{\mathrm{FWHM,\ Voigt}} \approx 0.5346\ \Gamma_{\mathrm{FWHM,\ Lorentz}} + \sqrt{0.2166\ \Gamma^2_{\mathrm{FWHM,\ Lorentz}} + \Gamma^2_{\mathrm{FWHM,\ Gauss}}}$$

where $\Gamma_{\mathrm{FWHM,\ Lorentz}} = 2\Gamma$ and $\Gamma_{\mathrm{FWHM,\ Gauss}} = 2\sigma\sqrt{2\ln(2)}$ ([20, 21]). In order to obtain a cut range equivalent to the 2σ-cut performed in the π^0-reconstruction the width is corrected by dividing by $\sqrt{2\ln(2)}$. The cut thus reads as

$$|m_{\pi^+\pi^0\pi^-} - m_\omega| \leq \Delta m = \frac{\Gamma_{\mathrm{FWHM,\ Voigt}}}{\sqrt{2\ln(2)}}$$

Only events with exactly one $\pi^+\pi^0\pi^-$-combination fulfilling this cut are retained.

The fit was applied from $700\,\mathrm{MeV/c^2}$ to $840\,\mathrm{MeV/c^2}$ with a fixed Lorentz width of $\Gamma = \Gamma_\omega = 8.4\,\mathrm{MeV/c^2}$, the ω decay width[12]. It yielded a mean value of $m_\omega = 783.4\,\mathrm{MeV/c^2}$ (PDG: $(782.7 \pm 0.1)\,\mathrm{MeV/c^2}$ [12]) and a standard deviation of $\sigma = 7.0\,\mathrm{MeV/c^2}$ which resulted in a cut range of $\Delta m = 23.1\,\mathrm{MeV/c^2}$. The resulting cut from $760.3\,\mathrm{MeV/c^2}$ to $806.5\,\mathrm{MeV/c^2}$ is consistent with the cut applied at VES, $758 \leq m_{\pi^+\pi^0\pi^-} \leq 808\,\mathrm{MeV/c^2}$[2].

A total of 198 268 $\pi^+\pi^0\pi^-$-combinations fulfilled the mass cut. Allowing only one good combination per event retained 149 070 combinations, corresponding to a ratio of 75% which matches well with the BNL result of 74%[1].

Figure 3.8 shows the obtained $\pi^+\pi^0\pi^-$ invariant mass spectrum including fit, mass cut and the finally selected unambiguous $\pi^+\pi^0\pi^-$-combinations. Apart from the ω-resonance there is also a small peak at about $550\,\mathrm{MeV/c^2}$, resulting from the decay $\eta \to \pi^+\pi^0\pi^-$ with a branching ratio of about 23%[12]. Figure 3.9 shows the invariant mass of the remaining $\pi^0\pi^-$-system after exactly one good ω has been found. The peak at around $770\,\mathrm{MeV/c^2}$ can be explained by the decay of $\rho(770)^-$-mesons.

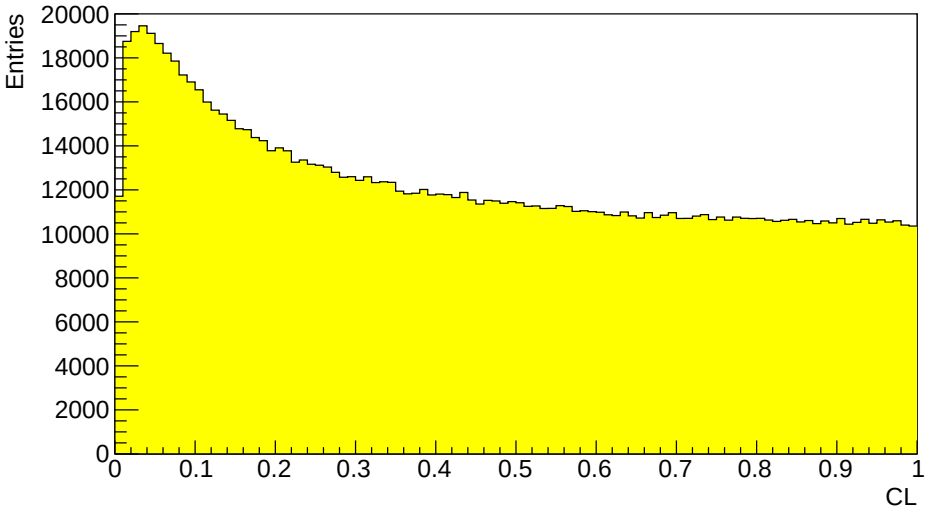

Fig 3.6: Confidence level distribution from the π^0 kinematic fit.

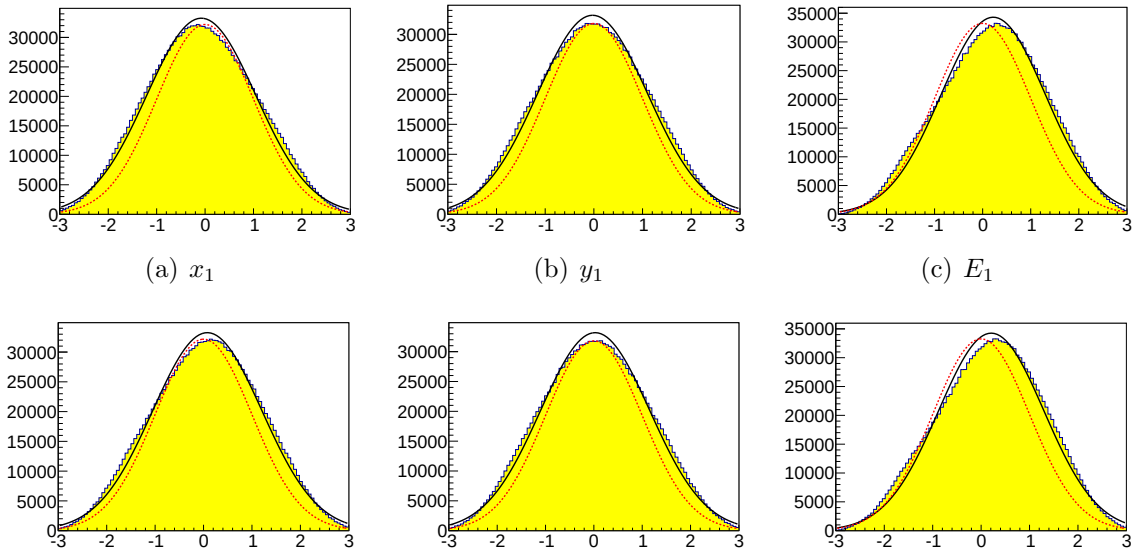

(a) x_1 (b) y_1 (c) E_1

(d) x_2 (e) y_2 (f) E_2

Fig 3.7: Pulls from the π^0 kinematic fit. The black curve shows a Gaussian fit. For comparison a 0-centered Gaussian with width of 1 is plotted in red.

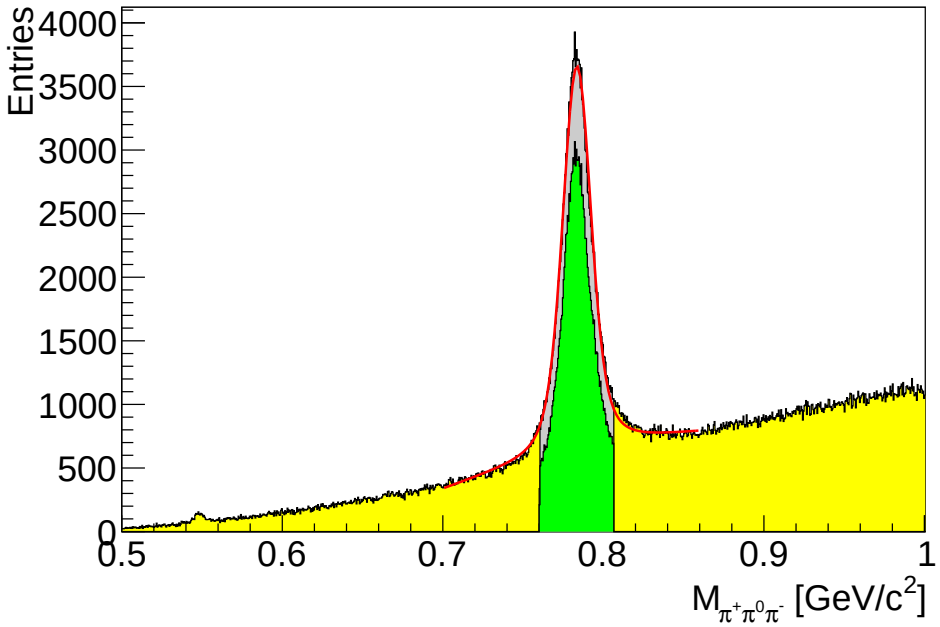

Fig 3.8: Invariant mass spectrum of the $\pi^+\pi^0\pi^-$-subsystem (4 entries per event). The grey area shows the cut $760.3\,\mathrm{MeV/c^2} \leq m_{\pi^+\pi^0\pi^-} \leq 806.5\,\mathrm{MeV/c^2}$, the green area the finally selected, unambiguous combinations. The fit is shown in red. The small peak at about $550\,\mathrm{MeV/c^2}$ results from the η-decay.

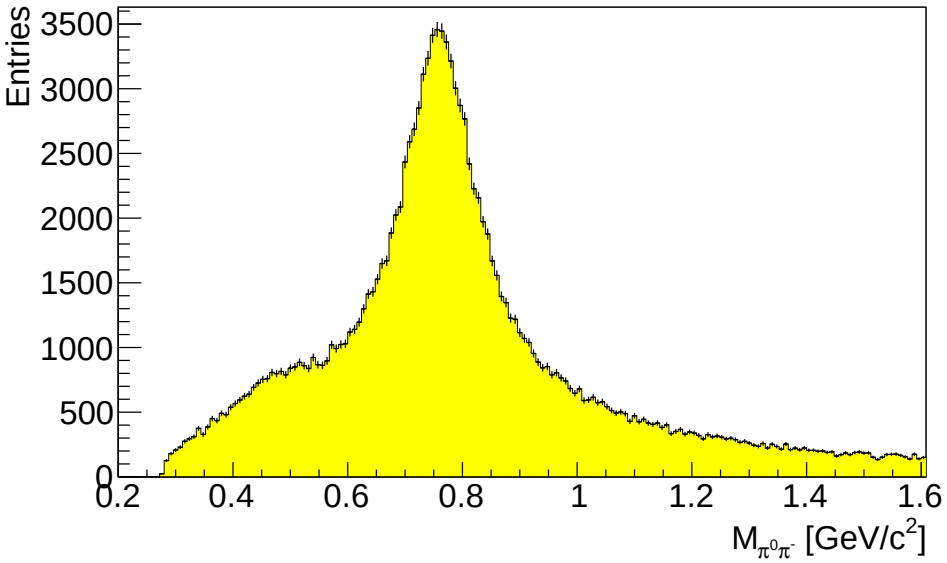

Fig 3.9: Invariant mass of $\pi^0\pi^-$-system after the succesful cut on exactly one good ω. The peak at around $770\,\mathrm{MeV/c^2}$ can be explained with the decay of $\rho(770)^-$-mesons.

$b_1(1235)$ Reconstruction After selecting events with exactly one ω-meson, the charged and neutral $b_1(1235)$ are reconstructed from

$$b_1(1235)^0 \to \omega + \pi^0 \quad \text{and} \quad b_1(1235)^- \to \omega + \pi^-$$

Because it is not possible to decide which decay was part of the measured intermediate state, both possibilities have to be considered. The obtained $\omega\pi$ invariant mass spectra are shown in figure 3.10.

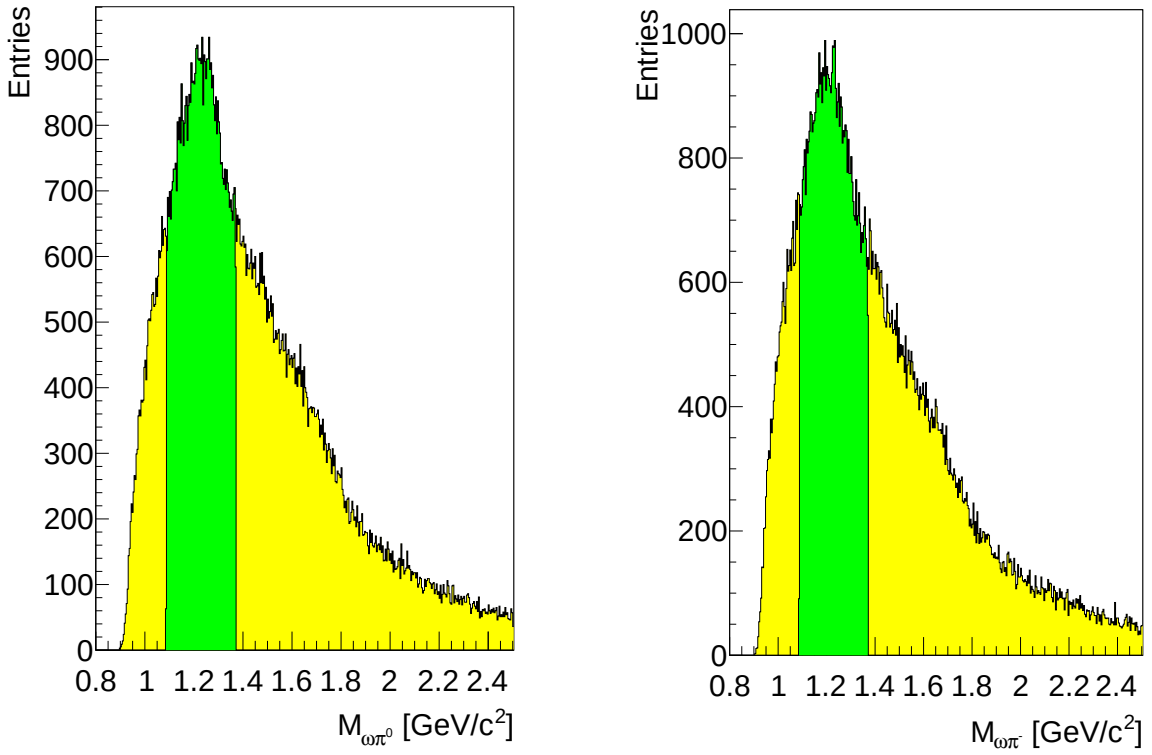

(a) $\omega\pi^0$ invariant mass spectrum

(b) $\omega\pi^-$ invariant mass spectrum

Fig 3.10: Invariant mass spectrum of $\omega\pi^0$ (potential neutral $b_1(1235)^0$) and $\omega\pi^-$ (potential negative $b_1(1235)^-$). The green areas mark the cut $|m_{\omega\pi} - 1230\,\mathrm{MeV/c^2}| \leq 142\,\mathrm{MeV/c^2}$.

These spectra show no clear $b_1(1235)$ peak. This is mainly due to the considerable width of the $b_1(1235)$ of about $\Gamma_{b_1(1235)} \approx 142\,\mathrm{MeV/c^2}$, the large (combinatorial) background and several other possible intermediate states with the same decay channel $X \to \omega\pi$. In order to inspect a $b_1(1235)\pi$ final state it is however necessary to select only $b_1(1235)$. The approach was to cut around the PDG value $m_{b_1(1235)} \approx 1230\,\mathrm{MeV/c^2}$ with a width of $\Delta m = \Gamma_{b_1(1235)} \approx 142\,\mathrm{MeV/c^2}$[12]. These cuts are indicated in green in the histogram. Obviously there is a large background that can not be neglected and will also be contained in the final mass spectra.

Resonance reconstruction The mass of the complete intermediate state X is easily calculated from all detected pions. Figure 3.11 shows the invariant mass spectrum without cutting on the $b_1(1235)$ mass, thus containing any decay via $X \to \omega\pi^0\pi^-$. There is a significant peak at about $1300\,\mathrm{MeV/c^2}$ which could be the decay of an $a_2(1320)^-$-meson with a mass of $1318\,\mathrm{MeV/c^2}$ and a branching fraction for the decay to $\omega\pi^0\pi^-$ of about 10% [12].

Further plots including cuts on the $\omega\pi$ invariant mass are shown in chapter 3.6, after a method to enhance statistics is presented in the next chapter.

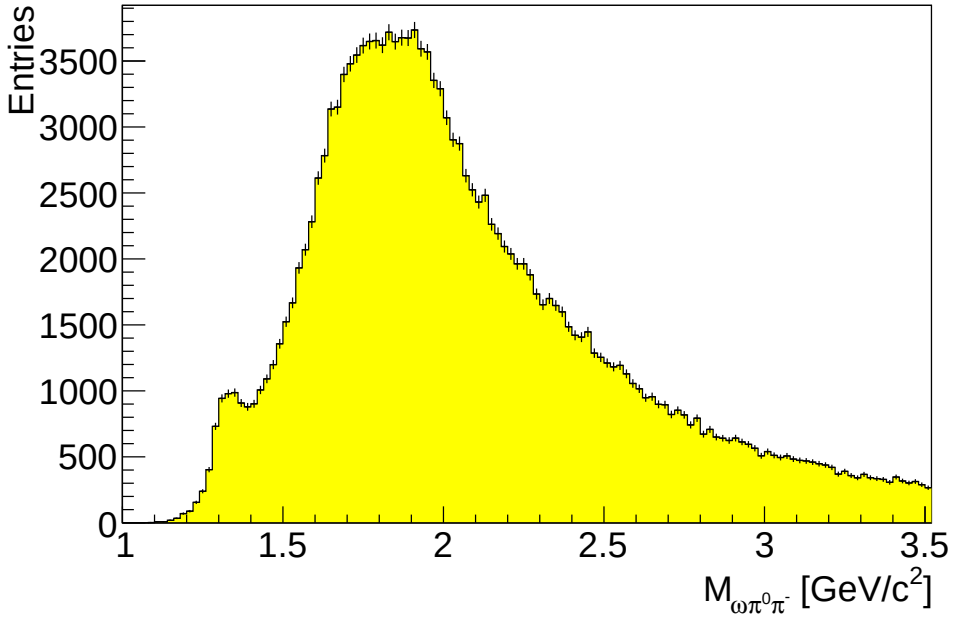

Fig 3.11: Total invariant mass without $b_1(1235)$-cuts

3.5 Events with Surplus Photons

Motivation As shown in chapter 3.1, the decay chain should only contain four gammas. Since there are also events with photons not associated with the corresponding reaction, for example due to pileup or noise in the calorimeters, it is possible to consider events with more than four photons. Taking this into account, the selection of gammas was widened to also include events with five or six gammas. Out of these photons all subsets of four photons are processed according to the procedure described in chapter 3.3. For each remaining 4γ-subset suitable associations to a $2\pi^0$-system are searched, as described in chapter 3.4. Only events where exactly one 4γ selection fulfills this $2\pi^0$-constraint are used. The remaining photons are discarded, so the subsequent analysis is identical to the normal 4-photon events.

The aim of this method is to enhance statistics in the considered decay channel. The method is limited by the decreasing signal-to-background ratio with additional gammas. Allowing more photons increases the probability to include events from other decays where a part of the final state has the same signature as the $b_1(1235)\pi$ intermediate state. Furthermore the combinatorial background increases severely since there are $\binom{N}{4}$ possibilities to select a 4γ-subset out of N photons.

Results Table 3.3 compares the number of found events with the number of good events for each photon count. The different columns mean:

- Gammas: Amount of good photons in the event.
- Before RPD-Cut: Amount of prefiltered events before RPD cuts (see chapter 3.3)
- $N(\pi^0\pi^-)$ $(N(\omega))$: Amount of events fulfilling the unambiguous $2\pi^0$ (ω)-cut.
- $R(\pi^0\pi^-)$ $(R(\omega))$: Ratio of events with more than one suitable $2\pi^0$ (ω) association to events with exactly one suitable $2\pi^0$ (ω) association.

The results show that the amount of good events relative to good 4γ-events is about 15% (five photons) and 6% (six photons), in sum enhancing the signal by 21%. The association of a 4γ-sample to two neutral pions becomes more ambiguous which also indicates that the amount of events with coincidentally suitable photon pairs increases. Both effects make clear that allowing even more photons is not advisable as the additionally gained statistics is very low, but the chances of including background increase.

Assuming that the events now selected from events with five or six photons are of the same nature as those from 4γ events, the quantity $R(\omega)$ should be same. As shown there is a small change which also indicates the decreased signal-to-background ratio.

Gammas	**Before RPD-Cut**	$\boldsymbol{N(\pi^0\pi^0)}$	$\boldsymbol{R(\pi^0\pi^0)}$	$\boldsymbol{N(\omega)}$	$\boldsymbol{R(\omega)}$
4	$1.26 \cdot 10^7$	$6.18 \cdot 10^5$	99.2%	$1.49 \cdot 10^5$	75.2%
5	$7.48 \cdot 10^6$	$1.16 \cdot 10^5$	87.8%	$2.29 \cdot 10^4$	76.6%
6	$4.43 \cdot 10^6$	$4.94 \cdot 10^4$	77.8%	$9.24 \cdot 10^3$	76.7%

Table 3.3: Comparison of amount of events containing four, five and six photons. A detailed description of the columns can be found in the text.

The signal-to-background ratio is illustrated in the 2γ invariant mass histogram used to select photon pairs from π^0-decays, shown in figure 3.12. For a better overview, the graphs were normalized to their peak values. Clearly the background increases significantly, whereas the peak width and position change hardly. The same fit as performed in chapter 3.4 returned mean values of $136.2\,\mathrm{MeV/c^2}$ in case of events with five and six photons, compared to $135.9\,\mathrm{MeV/c^2}$ in case of four photons. The standard deviation of $\sigma = 7.0\,\mathrm{MeV/c^2}$ was equal in all three cases, thereby indicating that this method yields reasonable results.

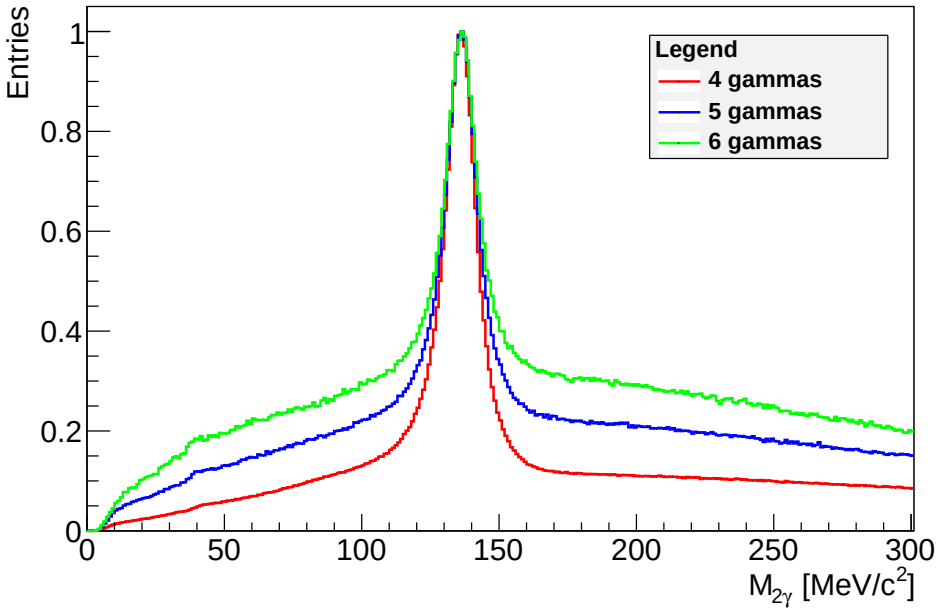

Fig 3.12: Comparison of the invariant 2γ-mass for events containing four, five and six gammas. The plots were normalized to their peak values.

Figure 3.13 compares the obtained $\omega\pi^0$ and $\omega\pi^-$ invariant mass spectra for events with four, five and six photons. In figure a) and b) the mass distributions for each photon count were normalized to the peak value in order to point out the general shapes. The fluctuations relative to the 4γ-curve are small in both cases, although they are significantly larger in the case of six photons than for five photons. This can be explained with both the lower statistics and the increasing background and is another hint that including even more photons is not advisable. Figures c) and d) compare the absolute numbers of good events in the mass spectra. The signal height is obviously improved, but the contribution of 6γ-events is already significantly smaller than for events containing only five photons, also showing that allowing more photons will hardly increase the statistics further.

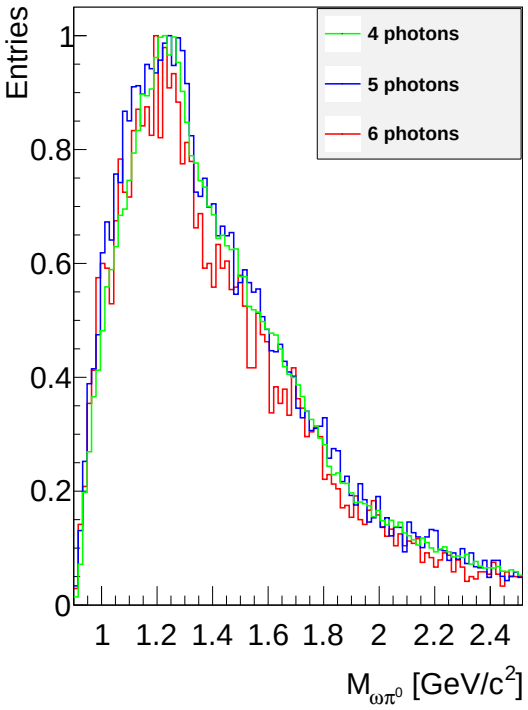

(a) $\omega\pi^0$ mass (normalized)

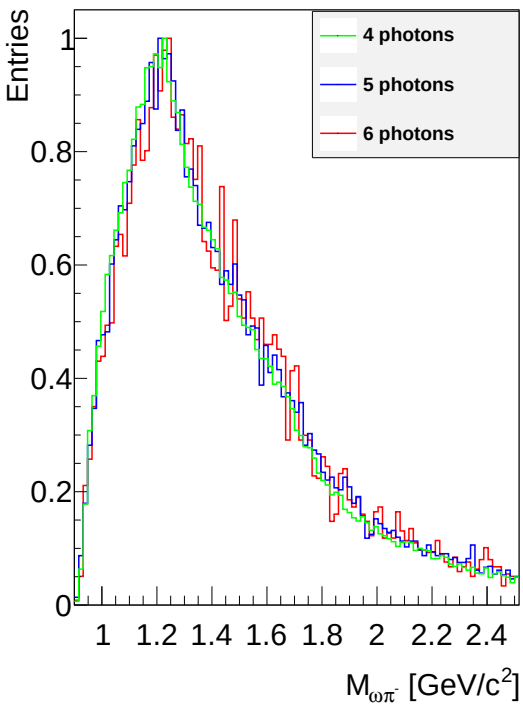

(b) $\omega\pi^-$ mass (normalized)

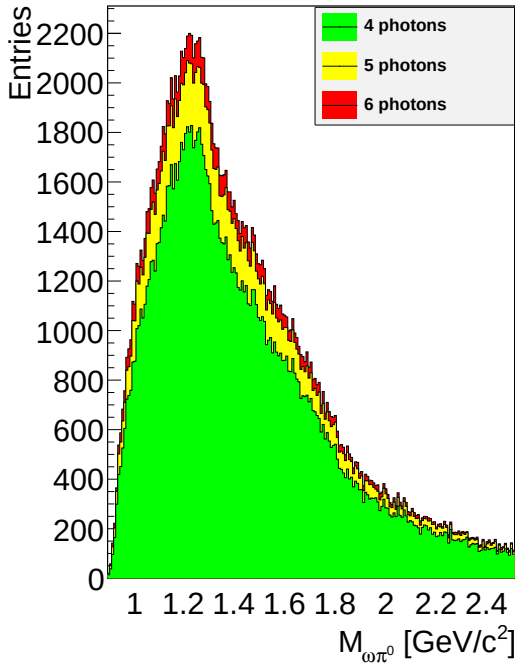

(c) $\omega\pi^0$ mass

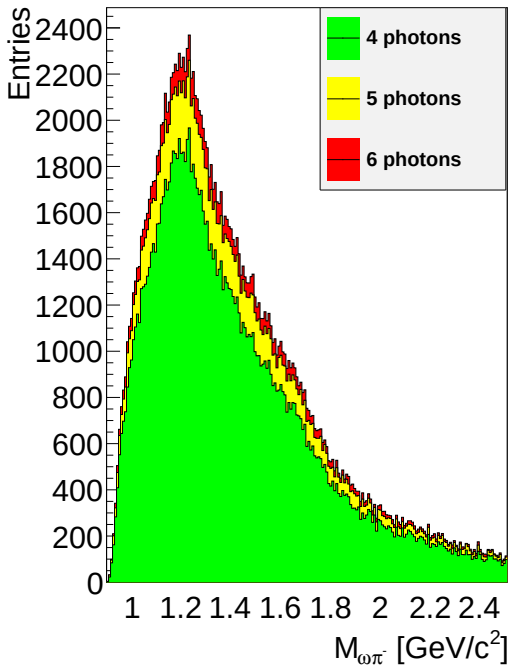

(d) $\omega\pi^-$ mass

Fig 3.13: Comparison of the $\omega\pi$ invariant mass spectra for events with 4, 5 and 6 photons. Figures a) and b) were normalized to the peak value to show the general shape of the plots, figures c) and d) show the absolute numbers. For better visibility, different binnings and colors were used.

3.6 Results

It was shown in the previous chapter that including events with five and six photons significantly increases the statistics. Therefore in the following all plots will contain the information gained from events with four to six photons.

Dalitz plots Dalitz plots of $m^2_{\omega\pi^-}$ against $m^2_{\omega\pi^0}$ from the decay $X \to \omega\pi^0\pi^-$ are shown in figure 3.14. Dalitz plots are only meaningful for small ranges in the mass of the decaying X, so mass regions of $(1300 \pm 50)\,\mathrm{MeV/c^2}$, $(1500 \pm 50)\,\mathrm{MeV/c^2}$, $(1600 \pm 50)\,\mathrm{MeV/c^2}$ and $(2000 \pm 50)\,\mathrm{MeV/c^2}$ were chosen, according to interesting regions in the total mass spectra shown afterwards. The expected horizontal and vertical structures at the $b_1(1235)$-mass are not visible because of the low statistics in each mass slice and the overlap with other resonances. Only a resonance along a 45° axis can be seen. Because for the shown Dalitz plots the variable $m^2_{\pi^0\pi^-}$ is constant along lines at 45° [22], this resonance results from $\rho(770)^-$-mesons which were also clearly seen in the $\pi^0\pi^-$ invariant mass spectrum (figure 3.9).

Comparison with BNL results The BNL experiment E852 has already published results of a partial-wave analysis of the investigated $b_1\pi$-channel. Figure 3.15 shows mass spectra from E852, namely the invariant masses of $\pi^+\pi^0\pi^-$ (ω candidates), $\omega\pi^0\pi^-$ (intermediate state X), remaining $\pi^0\pi^-$ after ω-cut and $\omega\pi^0$ ($b_1(1235)^0$ candidate). The corresponding plots from this analysis are shown in figure 3.16. In general, the obtained mass spectra at BNL and in this analysis show a similar shape. However, in this analysis the peaks from the ω and ρ-mesons are much clearer and have less background because of the better resolution of the COMPASS experiment. Furthermore the acceptance at COMPASS is larger than at E852, resulting in more events in the higher-mass regions.

Obtained total masses In the following the invariant mass spectra from the obtained intermediate states X are discussed for different combinations of the cuts on negative and neutral $b_1(1235)$.

The plot to be processed by a partial-wave analysis is shown in figure 3.17. In this case no cuts were applied to the $\omega\pi^0\pi^-$-sample. It shows a broad distribution with a clear peak at about $1300\,\mathrm{MeV/c^2}$ which could result from an $a_2(1320)^-$-decay. This meson with a mass of $1318\,\mathrm{MeV/c^2}$ decays to $\omega\pi^0\pi^-$ with a branching ratio of $10.6 \pm 3.2\%$[12].

Requiring a $b_1(1235)$ yields figure 3.18. The former peak at $1300\,\mathrm{MeV/c^2}$ decreases significantly due to the small phase space: the mass difference $\Delta m = m_{a_2(1320)} - m_{b_1(1235)} \approx 90\,\mathrm{MeV}$ is smaller than the mass of the remaining pion, so finding an $\omega\pi$-pair with an invariant mass near the $b_1(1235)$ mass is only possible because of the large widths of $a_2(1320)$ and $b_1(1235)$ and the broad cut range. Apart from this observation the plot differs from the previous one only in a slightly lower peak height and fewer events in the high-mass regions. The general shape has not changed significantly. Also drawn in the plot are the curves for the cut on a $b_1(1235)^0$ (red) and the cut on a $b_1(1235)^-$ (green). Clearly the histogram is not the sum of these both plots. The reason is that due to

the wide range of the cut on the $b_1(1235)$ invariant mass events can coincidentally fulfill both cuts. These events are shown in the blue curve. Its shape results from phase space limitations.

By demanding that exactly one of both cuts is fulfilled, thus selecting only events where a possible $b_1(1235)$ is unambiguous, we obtain figure 3.19. This plot again does not show significant changes in the high-mass region, but huge differences below $2\,\mathrm{GeV/c^2}$. At around $1.7\,\mathrm{GeV/c^2}$ a large gap is observed, as this is exactly the mass range where both cuts are often fulfilled simultaneously (see figure 3.18, blue curve). Since this method artificially cuts out a large mass region for $\omega\pi$-combinations these interesting results are from a physical point of view not useful for a deeper analysis.

Finally the total invariant mass with neither a negative nor a neutral $b_1(1235)$ is shown in figure 3.20. There is a clear peak at around $1.3\,\mathrm{GeV/c^2}$, probably from the remains of the $a_2(1320)$-decay, followed by a broad distribution. Similar to the previous cut a physical interpretation is difficult because again a large mass region for the final state is cut out.

Obtained statistics A total of 181 245 events were selected for the $\omega\pi^0\pi^-$ final states, in comparison to 145 148 events from the E852 analysis [1]. Considering that period W37 contains only about 38% of the total data from 2008 [23], about 480 000 events can be expected from the total data set, thus increasing statistics greatly.

Table 3.4 shows the amount of $\omega\pi^0\pi^-$ final states in the mass range of the above plots, $1 \leq m_{\omega\pi^0\pi^-} \leq 3.5\,\mathrm{GeV/c^2}$, for each histogram. Although the cut on the $b_1(1235)$ invariant mass cannot be chosen very precisely, these numbers indicate that there is a considerable component of $b_1(1235)\pi$-decays in the selected final state. Thus the COMPASS experiments provides an excellent data sample for the verification of spin-exotic particles.

	No cuts applied	**At least one cut fulfilled**	**Only one cut fulfilled**	**No cuts fulfilled**
Events	179 011	109 691	80 217	69 320
Percentage	100%	61.3%	44.8%	38.7%

Table 3.4: Amount of final states with respect to $b_1(1235)$-cuts in the range of $1 \leq m_{\omega\pi^0\pi^-} \leq 3.5\,\mathrm{GeV/c^2}$

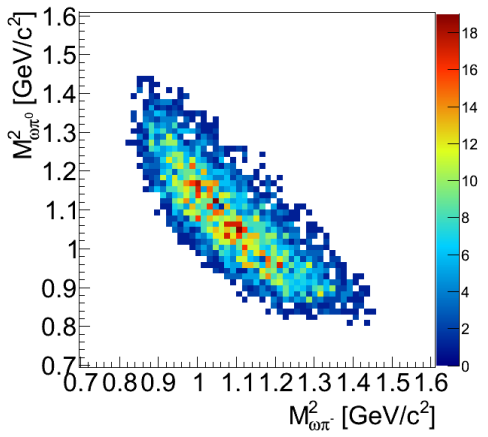

(a) $m_{\text{total}} = (1300 \pm 50)\,\text{MeV/c}^2$

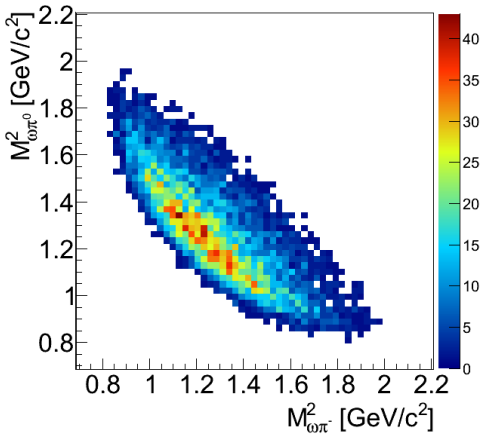

(b) $m_{\text{total}} = (1500 \pm 50)\,\text{MeV/c}^2$

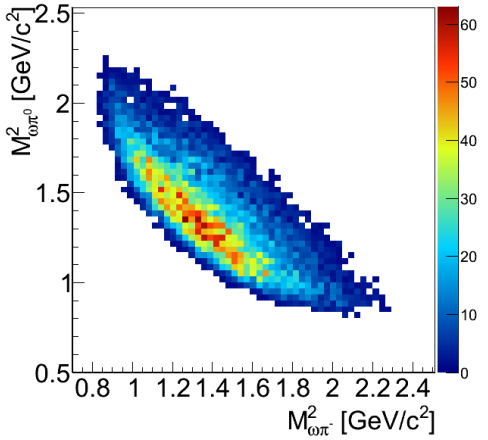

(c) $m_{\text{total}} = (1600 \pm 50)\,\text{MeV/c}^2$

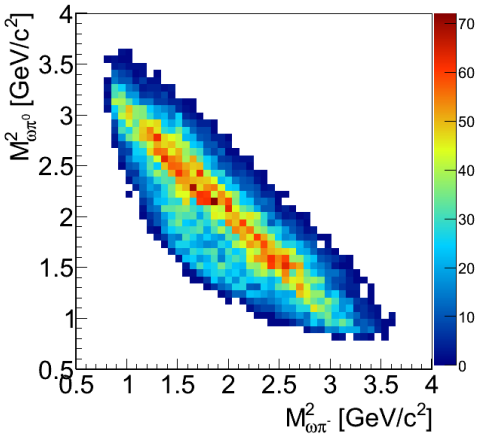

(d) $m_{\text{total}} = (2000 \pm 50)\,\text{MeV/c}^2$

Fig 3.14: Dalitz plots of $m^2_{\omega\pi^-}$ against $m^2_{\omega\pi^0}$ for different regions of the total invariant mass.

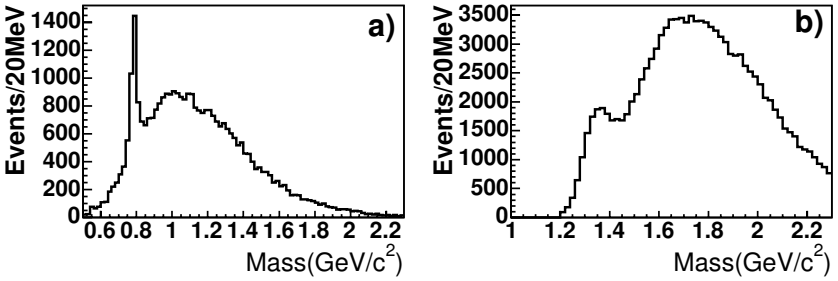

(a) $\pi^+\pi^0\pi^-$ mass before ω-cut (all combinations)

(b) $\omega\pi^0\pi^-$ mass

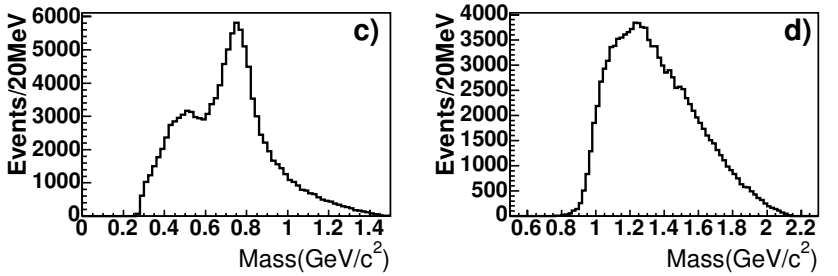

(c) remaining $\pi^0\pi^-$ mass after ω-cut

(d) $\omega\pi^0$ mass

Fig 3.15: Invariant masses from the BNL-E852 analysis[1].

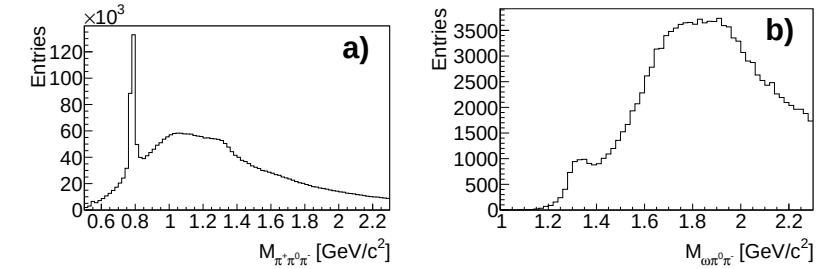

(a) $\pi^+\pi^0\pi^-$ mass before ω-cut (all combinations)

(b) $\omega\pi^0\pi^-$ mass

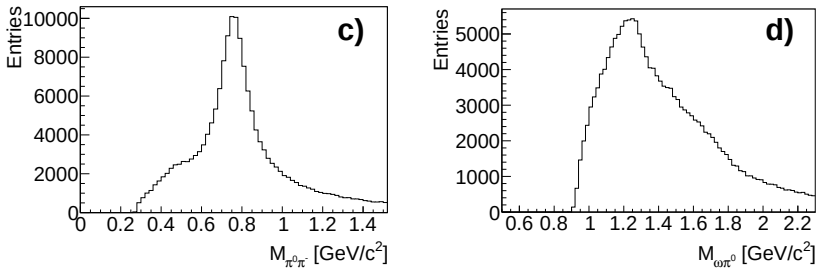

(c) remaining $\pi^0\pi^-$ mass after ω-cut

(d) $\omega\pi^0$ mass

Fig 3.16: Comparison plots to the BNL-E852 analysis.

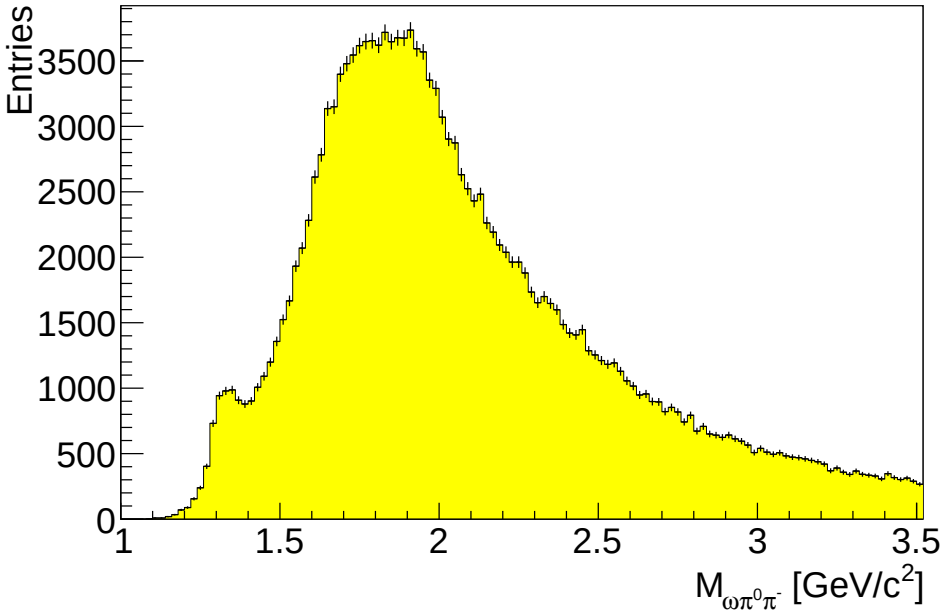

Fig 3.17: Total invariant mass without applying the $b_1(1235)$-cuts

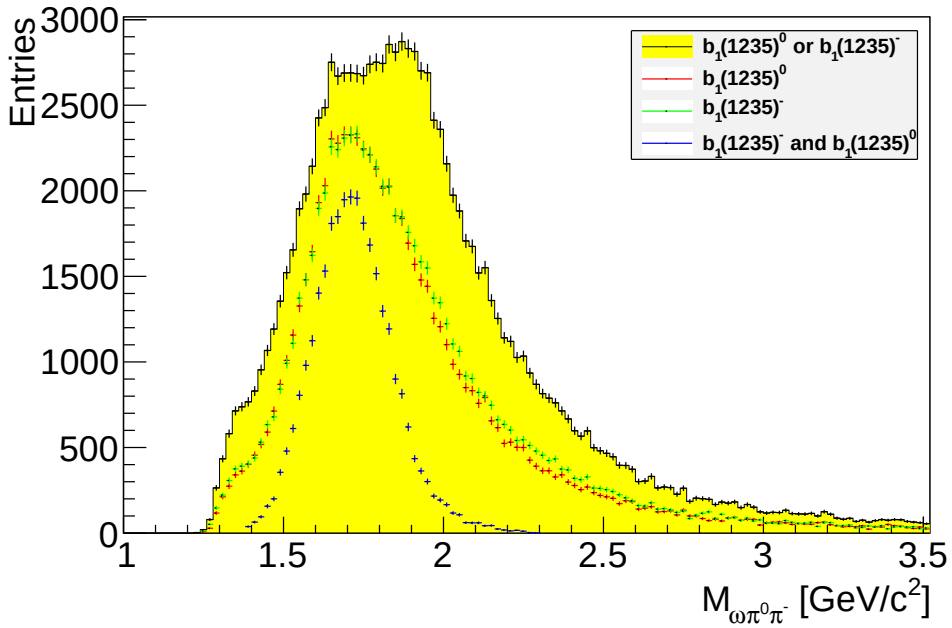

Fig 3.18: Total invariant mass of events fulfilling the negative or the neutral $b_1(1235)$-cut. The red line represents events where the $b_1(1235)^0$-cut is fulfilled, the green line events where the $b_1(1235)^-$-cut is fulfilled and the blue line events where both cuts are fulfilled.

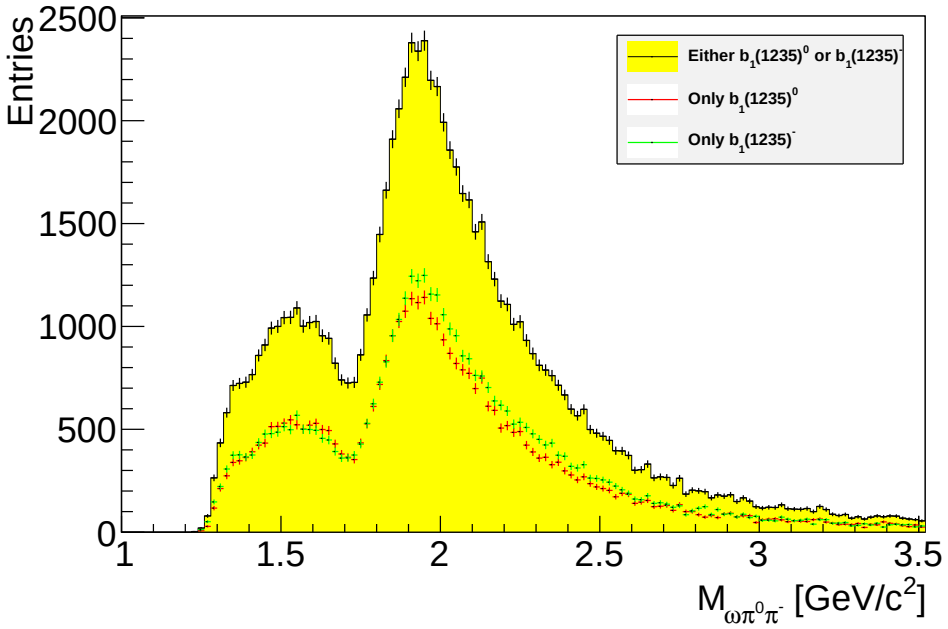

Fig 3.19: Total invariant mass of events fulfilling either the negative or the neutral $b_1(1235)$-cut. The red line represents events where only the $b_1(1235)^0$-cut is fulfilled, the green line events where only the $b_1(1235)^-$-cut is fulfilled.

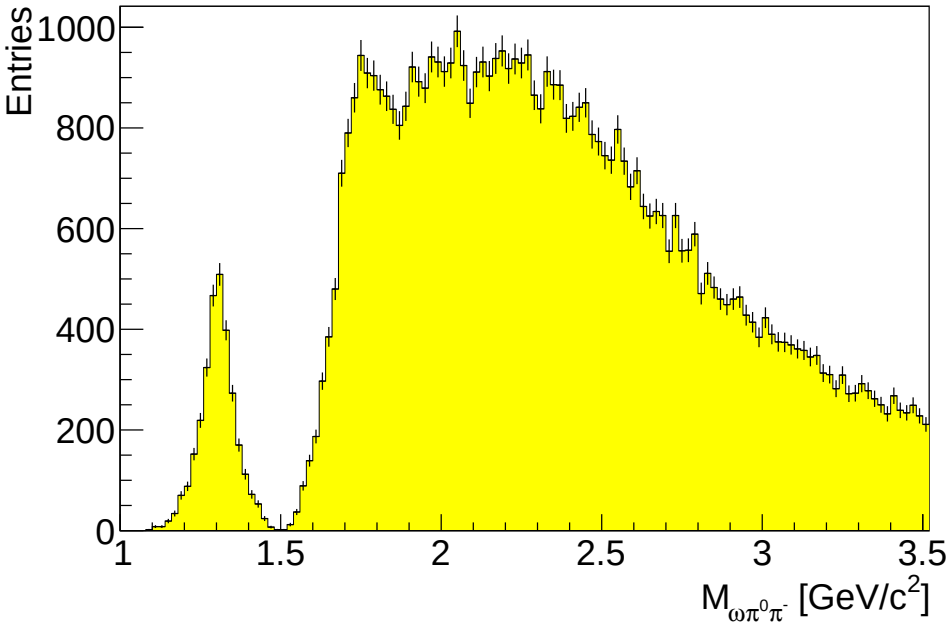

Fig 3.20: Total invariant mass of events fulfilling neither the negative nor the neutral $b_1(1235)$-cut.

4 Summary and Conclusion

In order to investigate spin-exotic mesons, one of the goals at the COMPASS experiment, partial-wave analyses (PWA) of promising decay channels are necessary. The spin-exotic $\pi_1(1600)$ was seen at VES and BNL-E852 in the analysis of $b_1(1235)\pi$ final states. E852 also found signs of $\pi_1(2000)$-mesons. The focus of this thesis is to reconstruct the $b_1(1235)\pi$ final state in COMPASS data for a following PWA to verify these results. The data from period W37 of the 2008 COMPASS hadron run was examined for the diffractive pion scattering off protons in which the $b_1(1235)\pi$ intermediate states was created. The reconstruction of the total decay chain leads to the final state $\pi^+2\pi^0 2\pi^-$.

The basic event selection consists of cuts on the DT0 trigger, the location of the primary vertex and the correct amount of outgoing particles. To retain only exclusively measured events cuts on the momentum distribution and the total energy of the intermediate state X and the detected recoil proton were applied. The lack of a good calibration of the electromagnetic calorimeters was compensated by a calibration of the reconstructed clusters. In the following $2\pi^0$-reconstruction all possible combinations of photon-pairs were regarded and events with more than one suitable combination were discarded. Afterwards kinematic fitting was used to correct the mass deviation from the PDG value due to the detector resolution. For the $\omega \to \pi^+\pi^0\pi^-$ decay reconstruction from the $\pi^+2\pi^0 2\pi^-$-system, it was again requested that only one $\pi^+\pi^0\pi^-$ combination lies in the ω-mass window. The cuts on $m_{2\gamma}$ and $m_{\pi^+\pi^0\pi^-}$ were determined from fits of the obtained invariant mass spectra from all combinations. The neutral and negative $b_1(1235)$ reconstructed from $\omega\pi$ show no clear peaks in the invariant mass spectra, thus the approach to cut around the PDG reference mass with the corresponding decay width was used to select $b_1(1235)$. The invariant mass of the total final state which will be used in the future for a PWA was finally determined without $b_1(1235)$-cuts and with at least one fulfilled cut. Other combinations of these cuts also show interesting results.

To enhance the signal, events with five and six photons were also allowed, excluding photons assumed to result from pileup or noise. This method yielded a signal gain of about 20%, but also showed that including more than six photons is not advisable.

In comparison to the BNL results the COMPASS data showed a good accordance, but thanks to the better resolution and larger acceptance particle resonances are clearer with less background and more events are found in the high-mass regions. Considering the larger reconstructed dataset COMPASS is in an excellent position to verify the PWA results from BNL and VES.

In order to further enhance the analysis the total 2008 dataset could be used, increasing the obtained statistics by a factor of about 2.6. An improvement of the calorimeter calibration will be made to further reduce the background. Another interesting analysis would be the investigation of the ρ-meson clearly seen in the $\pi^0\pi^-$ mass spectrum.

List of Figures

List of Tables

Bibliography

[1] M. Lu et al. Exotic meson decay to $\omega\pi^0\pi^-$. *Phys. Rev. Lett.*, 94(3):032002, Jan 2005.

[2] Valery Dorofeev (for VES Collaboration). The $J^{PC} = 1^{-+}$ hunting season at VES. *AIP Conference Proceedings*, 619(1):143–154, 2002.

[3] Frank Nerling for the COMPASS Collaboration. First Results on Hadron Spectroscopy at COMPASS. (arXiv/1012.4993), 2010.

[4] COMPASS Collaboration, P. Abbon et al. The COMPASS Experiment at CERN. oai:cds.cern.ch:1028264. *Nucl. Instrum. Methods Phys. Res., A*, 577(arXiv:hep-ex/0703049. CERN-PH-EP-2007-001. 3):455–518. 84 p, Jan 2007.

[5] COMPASS Collaboration. The COMPASS Setup for Physics with Hadron Beams. (Publication in process), 2011.

[6] Stefan Pflüger. private communications, 2011.

[7] Hauke Wöhrmann. Diffraktive Produktion von Dreikörper-Endzuständen in π^-p-Wechselwirkung am COMPASS-Experiment (CERN). Diploma Thesis, October 2010.

[8] ProtonTrigger. `http://wwwcompass.cern.ch/twiki/bin/view/Detectors/ProtonTrigger`, 15.07.2011.

[9] Johannes Bernhard. The COMPASS Recoil Proton Detector. DPG Spring Meeting 2009 Bochum.

[10] Sabine Dinter. Analysis of Final States with π and η Mesons produced in π^-p Interactions and Studies of the Electromagnetic Calorimeters at COMPASS (CERN). Diploma Thesis, March 2010.

[11] F. Haas et al. Diffractive Dissociation into $\pi^-\pi^-\pi^+$ Final States at COMPASS, Version 2. COMPASS Release Note 2009.

[12] K. Nakamura et al. (Particle Data Group). J. Phys. G 37, 075021 (2010) and 2011 partial update for the 2012 edition.

[13] COMPASS software pages. `http://wwwcompass.cern.ch/compass/software/offline/`, 06.07.2011.

[14] CORAL. `https://twiki.cern.ch/twiki/bin/view/Persistency/Coral`, 06.07.2011.

[15] ROOT. `http://root.cern.ch/drupal/content/about`, 06.07.2011.

[16] PHysics Analysis Software Tools. `http://ges.web.cern.ch/ges/phast/index.html`, 06.07.2011.

[17] HadronTrigger. `http://compass02.cern.ch/twiki/bin/view/Trigger/HadronTrigger`, 06.07.2011.

[18] Tobias Schlüter. Neutral final states in 2008 π^- data. COMPASS Meeting March 18-19, 2009.

[19] Tobias Schlüter. A code for kinematic fitting with constraints from intermediate particle masses. COMPASS Note 2007-10, 2009.

[20] Voigt profile - Wikipedia. `http://en.wikipedia.org/wiki/Voigt_profile`, 19.07.2011.

[21] J.J. Olivero and R.L. Longbothum. Empirical fits to the voigt line width: A brief review. *Journal of Quantitative Spectroscopy and Radiative Transfer*, 17(2):233–236, 1977.

[22] Dalitz Plot. `http://rd11.web.cern.ch/RD11/rkb/PH14pp/node39.html`, 20.07.2011.

[23] Boris Grube. private communications, 2011.

Acknowledgements

First of all I would like to thank Prof. Stephan Paul for giving me this interesting subject. Working in his group always was a pleasure.

My sincerest thanks to Dr. Boris Grube for his permanent helpfulness. His patient and competent support helped to accomplish this thesis and made me learn a lot about data analysis. The continuous exchange of ideas with him greatly supported the development of central ideas in this thesis.

I would also like to thank the members of E18 for the nice atmosphere and willingness to help, especially Stefan Pflüger and Tobias Schlüter for their quick responses to any of my questions.

Finally I am very grateful for my parents who always supported me during my studies.